Available on CMS information server

CMS NOTE 2006/140

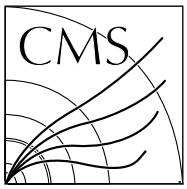

The Compact Muon Solenoid Experiment

CMS Note

Mailing address: CMS CERN, CH-1211 GENEVA 23, Switzerland

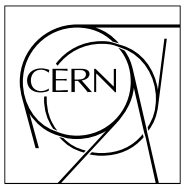

27th September 2006

Energy resolution performance of the CMS electromagnetic calorimeter

P. Adzic[3], R. Alemany-Fernandez[13], C.B. Almeida[13,14], N.M. Almeida[13], G. Anagnostou[2], M.G. Anfreville[11], I. Anicin[3], Z. Antunovic[30], E. Auffray[10], S. Baccaro[28,29], S. Baffioni[25], D. Barney[10], L.M. Barone[29], P. Barrillon[15], A. Bartoloni[29], S. Beauceron[11], F. Beaudette[10], K.W. Bell[8], R. Benetta[10], M.J. Bercher[25], U. Berthon[25], B. Betev[38], R. Beuselinck[15], A. Bhardwaj[7], C. Biino[33], S. Bimbot[25], J. Blaha[35], P. Bloch[10], S. Blyth[6], P. Bordalo[13], A. Bornheim[26], J.M. Bourotte[25,10], D. Britton[15], R.M. Brown[8], R. Brunelière[10], P. Busson[25], T. Camporesi[10], N. Cartiglia[33], F. Cavallari[29], M. Cerutti[25], D. Chamont[25], P. Chang[6], Y.H. Chang[6], C. Charlot[25], S. Chatterji[7], E.A. Chen[6], R. Chipaux[11], B.C. Choudhary[7], D.J. Cockerill[8], C. Collard[25], C. Combaret[35], F. Cossutti[34], S. Costantini[29], J.C. Da Silva[13], I. Dafinei[29], G. Daskalakis[15], G. Davatz[38], A. Debraine[25], D. Decotigny[25], A. De Min[17], K. Deiters[36], M. Dejardin[11], R. Della Negra[35], G. Della Ricca[34], P. Depasse[35], J. Descamp[11], G. Dewhirst[15], S. Dhawan[23], M. Diemoz[29], G. Dissertori[38], M. Dittmar[38], L. Djambazov[38], L. Dobrzynski[25], S. Drndarevic[3], M. Dupanloup[35], M. Dzelalija[30], J. Ehlers[38], H. El Mamouni[35], A. Elliott-Peisert[10], I. Evangelou[12], B. Fabbro[11], J.-L. Faure[11], J. Fay[35], F. Ferri[17], P.S. Flower[8], G. Franzoni[17,18], W. Funk[10], A. Gaillac[25], C. Gargiulo[29], S. Gascon Shotkin[35], Y. Geerebaert[25], F.-X. Gentit[11], A. Ghezzi[17], J. Gilly[25], A.-S. Giolo-Nicollerat[38,10], A. Givernaud[11], S. Gninenko[20], A. Go[6], N. Godinovic[31], N. Golubev[20], I. Golutvin[9], R. Gomez-Reino[10], P. Govoni[17], J. Grahl[18], P. Gras[11], J. Greenhalgh[8], J.-P. Guillaud[1], M. Haguenauer[25], G. Hamel-de-Montechenault[11], M. Hansen[10], H.F. Heath[5], J.A Hill[8], P.R. Hobson[16], D. Holmes[5], A.G. Holzner[38], G.W. Hou[32], B. Ille[35], Q. Ingram[36], A. Jain[13], P. Jarry[11], C. Jauffret[25], M. Jha[7], A. Karar[25], S.K. Kataria[22], V. Katchanov[27], B.W. Kennedy[8], K. Kloukinas[10], P. Kokkas[12], M. Korjik[19], N. Krasnikov[20], D. Krpic[3], A. Kyriakis[2], M. Lebeau[10], P. Lecomte[38], P. Lecoq[10], M.-C. Lemaire[11], M. Lethuillier[35], W. Lin[6], A.L. Lintern[8], A. Lister[38], V. Litvin[26], E. Locci[11], A.B. Lodge[8], E. Longo[29], D. Loukas[2], D. Luckey[38], W. Lustermann[38], C. Lynch[5], C.K. Mackay[5], M. Malberti[17], D. Maletic[3], I. Mandjavidze[11], N. Manthos[12], A. Markou[2], H. Mathez[35], A. Mathieu[25], V. Matveev[20], G. Maurelli[35], E. Menichetti[33], P. Meridiani[29], P. Milenovic[3], G. Milleret[25], P. Mine[25], M. Mur[11], Y. Musienko[4,19], A. Nardulli[38], J. Nash[15,10], H. Neal[23], P. Nedelec[1], P. Negri[17], F. Nessi-Tedaldi[38], H.B. Newman[26], A. Nikitenko[15], M.M. Obertino[33,18], R.A. Ofierzynski[10,38], G.C. Organtini[29], P. Paganini[25], M. Paganoni[17], I. Papadopoulos[12], R. Paramatti[10,29], N. Pastrone[33], F. Pauss[38], P. Poilleux[25], I. Puljak[31], A. Pullia[17], J. Puzovic[3], S. Ragazzi[17], S. Ramos[13], S. Rahatlou[29], J. Rander[11], K. Ranjan[7], O. Ravat[35], M. Raymond[15], P.A. Razis[24], N. Redaelli[17], D. Renker[36], S. Reucroft[4], J.M. Reymond[11], M. Reynaud[35], S. Reynaud[10], T. Romanteau[25], F. Rondeaux[11], A. Rosowsky[11], C. Rovelli[17], P. Rumerio[10], R. Rusack[18], S.V. Rusakov[21], M.J. Ryan[15], H. Rykaczewski[38], T. Sakhelashvili[36,39], R. Salerno[17], M. Santos[13,14], C. Seez[15], I. Semeniouk[25], O. Sharif[16], P. Sharp[15], C. Shepherd-Themistocleous[8], S. Shevchenko[26], R.K. Shivpuri[7], G. Sidiropoulos[12], D. Sillou[1], A. Singovski[18], Y. Sirois[25], A.M. Sirunyan[37], B. Smith[8], V.J. Smith[5], M. Sproston[8], H. Suter[38], J. Swain[4], T. Tabarelli De Fatis[17], M. Takahashi[15], R.J. Tapper[5], A. Tcheremoukhine[9], I. Teixeira[13,14], J.P. Teixeira[13,14], O. Teller[10], C. Timlin[15], F.A Triantis[12], S. Troshin[27], N. Tyurin[27], K. Ueno[32], A. Uzunian[27], J. Varela[13,10], N. Vaz Cardoso[13], P. Verrecchia[11], P. Vichoudis[10], S. Vigano[17], G. Viertel[38], T. Virdee[15,10], E. Vlassov[10,40], M. Wang[32], A. Weinstein[26], J.H. Williams[8], I. Yaselli[16], A. Zabi[15], N. Zamiatin[9], S. Zelepoukine[27,38], M. Zeller[23], L.Y. Zhang[26], Y. Zhang[15], K. Zhu[26] and R.Y. Zhu[26]

Abstract

The energy resolution performance of the CMS lead tungstate crystal electromagnetic calorimeter is presented. Measurements were made with an electron beam using a fully equipped supermodule of the calorimeter barrel. Results are given both for electrons incident on the centre of crystals and for electrons distributed uniformly over the calorimeter surface. The electron energy is reconstructed in matrices of 3×3 or 5×5 crystals centred on the crystal containing the maximum energy. Corrections for variations in the shower containment are applied in the case of uniform incidence. The resolution measured is consistent with the design goals.

[1] Laboratoire d'Annecy-le-Vieux de Physique des Particules, 74941 Annecy-le-Vieux, France
[2] Institute of Nuclear Physics "Demokritos", 153 10 Attiki, Greece
[3] "Vinca" Institute of Nuclear Sciences and Faculty of Physics of University of Belgrade, 11000 Belgrade, Serbia and Montenegro
[4] Northeastern University, Boston MA 02115-5096, USA
[5] Bristol University, Bristol BS8 1TL, United Kingdom
[6] National Central University, Chung-Li, Taiwan, ROC
[7] Delhi University, Delhi 110 007, India
[8] CCLRC, Rutherford Appleton Laboratory, Didcot OX11 0QX, United Kingdom
[9] Joint Institute for Nuclear Research, 141980 Dubna (Moscow Region), Russia
[10] European Organization for Nuclear Research, CERN, 1211 Geneva 23, Switzerland
[11] CEA/Saclay, 91191 Gif-sur-Yvette cedex, France
[12] University of Ioannina, 451 10 Ioannina, Greece
[13] Laboratório de Instrumentação e Fsica Experimental de Partículas, 1000-149 Lisboa, Portugal
[14] Instituto de Engenharia de Sistemas e Computadores, 1000-029 Lisboa, Portugal
[15] Imperial College, London SW7 2BZ, United Kingdom
[16] Brunel University, Middlesex UB8 3PH, United Kingdom
[17] Università degli Studi Milano-Bicocca and INFN- Sezione di Milano, 20126 Milano, Italy
[18] University of Minnesota, Minneapolis MN 55455, USA
[19] Research Institute for Nuclear Problems, Byelorussian State University, 220050 Minsk, Byelorussia
[20] Institute for Nuclear Research, Russian Academy of Sciences, 117312 Moscow, Russia
[21] Lebedev Physical Institute, Russian Academy of Sciences, 117924 Moscow, Russia
[22] Bhabha Atomic Research Centre, Mumbai 400 085, India
[23] Yale University, New Haven CT 06520-8121, USA
[24] Cyprus University, 1678 Nicosia, Cyprus
[25] Laboratoire Leprince-Ringuet, Ecole Polytechnique, 91128 Palaiseau Cedex, France
[26] California Institute of Technology, Charles C. Lauritsen Laboratory, Pasadena CA91125, USA
[27] State Research Center, 142284 Protvino (Moscow Region), Russia
[28] ENEA - CR Casaccia, 00060 S. Maria di Galeria, Roma, Italy
[29] Università "La Sapienza", Dipartimento di Fisica and INFN-Sezione di Roma, 00185 Roma, Italy
[30] Split University, PMF, 21000 Split, Croatia
[31] Technical University of Split, FESB, 21000 Split, Croatia
[32] National Taiwan University, 106 Taipei, Taiwan ROC
[33] Università di Torino, Dipartimento di Fisica and INFN-Sezione di Torino, 10125 Torino, Italy
[34] Università di Trieste, Dipartimento di Fisica and INFN-Sezione di Trieste, 34127 Trieste, Italy
[35] Institut de Physique Nucléaire, IN2P3-CNRS and Université C. Bernard Lyon I, 69622 Villeurbanne, France
[36] Paul Scherrer Institut, 5232 Villigen, Switzerland
[37] Yerevan Physics Institute, 375036 Yerevan 36, Armenia
[38] Institute for Particle Physics, ETH Zürich, 8093 Zürich, Switzerland
[39] On leave from High Energy Physics Institute, Tblisi, Georgia
[40] Institute for Theoretical and Experimental Physics, RU-117259 Moscow

1 Introduction

The Compact Muon Solenoid (CMS) experiment [1] is a general purpose detector which will operate at the LHC proton-proton collider at CERN. The experiment is equipped with a hermetic homogeneous electromagnetic calorimeter (ECAL) [2] made of lead tungstate ($PbWO_4$) crystals. The crystal material has been chosen for its fast response and its resistance to irradiation as well as its high density (8.3 g/cm^3), short radiation length ($X_0 \simeq 0.89$ cm) and small Moliere radius ($R_M \simeq 2.19$ cm), allowing a compact detector to be built. The ECAL was designed to provide the granularity and the excellent energy resolution which is required, in particular, to detect the postulated Standard Model Higgs boson via the two photon decay mode.

The barrel of the ECAL is divided into two halves, each composed of 18 supermodules containing 1700 crystals. The individual crystals have a truncated-pyramid shape with a lateral size of approximately $1 \times R_M$ and a length of $25.8X_0$. The crystals are organized in a quasi-projective geometry, their principal axes making a 3° angle with respect to a vector from the nominal proton-proton interaction vertex, in both the azimuthal and polar angle projections [3].

Extensive measurements were carried out with one supermodule during a test beam campaign on the H4 beam line at CERN in October and November 2004. The supermodule was exposed to electrons with energies between 20 and 250 GeV. In this paper, the energy resolution performance of the ECAL is discussed. The calorimeter response is reconstructed by summing the energy deposits in matrices of either 3×3 or 5×5 crystals. Results are presented both for the cases of central and uniform incidence of the electrons on the crystals.

2 Experimental set up

The ECAL supermodule was installed on the H4 beam line on a movable table. The table could rotate in the polar angle (horizontal plane) and azimuthal angle (vertical plane) thus allowing the electron beam to be directed at crystals in all parts of the supermodule. The beam electrons were incident at an angle of $\simeq 3^\circ$ (in both transverse planes) to the direction of the crystal principal axis to reproduce the average incident angle of the particle with respect to the ECAL during LHC running. The transverse incidence position of the beam electrons was determined by four planes of scintillating fibre hodoscopes situated upstream of the movable table.

The supermodule was fully equipped with the final readout electronics [3], briefly described in Section 3, as well as with the final high and low voltage regulation, cooling, and temperature monitoring systems [4, 5, 6], and laser monitoring system [7].

Plastic scintillator counters were used to trigger the readout of the supermodule crystals. The trigger defines an area of 20×20 mm^2, slightly smaller than the front faces of the crystals ($\simeq$22 $\times$ 22 mm^2).

3 Readout and Reconstruction

The light produced in each crystal of a supermodule is detected via a pair of avalanche photodiodes. Each crystal is read out independently. The readout proceeds via a Multi Gain Pre-Amplifier (MGPA) with 3 parallel gain stages (with nominal gains of 12, 6, and 1), each followed by an Analog to Digital Converter (ADC). The data from the channel with non-saturated ADC and which has the highest gain is then read out.

The crystal scintillation signals are digitized continuously at 40 MHz. At the test beam, the phase of the trigger time relative to the digitization clock was measured with a time-to-digital converter. The signal amplitude is reconstructed from up to five consecutive digitization samples. The reconstruction uses a method implementing a digital filter which minimizes the contribution of the electronics noise [8].

A measurement of the noise in the ECAL supermodule for a single crystal and for crystal arrays is presented in Section 3.1. The amplitude reconstruction over the range of incident electron energies used requires the determination of the ratio of MGPA gains. This is discussed in Section 3.2.

3.1 Measurement of the signal noise

A measurement of the electronics noise is made by applying the amplitude reconstruction procedure to data (pedestal events) taken with a random trigger, in the absence of an electron signal. Pedestal subtracting weights [8] are used for the amplitude reconstruction. This method makes use of three signal samples measured before the pulse, to perform a subtraction of the pedestal on an event-by-event basis.

The distribution of reconstructed amplitudes for an individual channel is shown in Fig. 1a. The width of this distribution obtained from a Gaussian fit is a measure of the noise. The distribution of such noise measurements for a large number of individual channels is shown in Fig. 1b. Due to fast control problems, about 25% of the channels

could not be reliably read out. The mean noise in a single channel is found to correspond to a signal dispersion of 41.5 MeV. Figures 1c and 1d show the distribution of the measured noise in matrices of 3×3 and 5×5 crystals. On average, a noise equivalent to about 127 MeV is measured for the 3×3 matrices, and 213 MeV for the 5×5

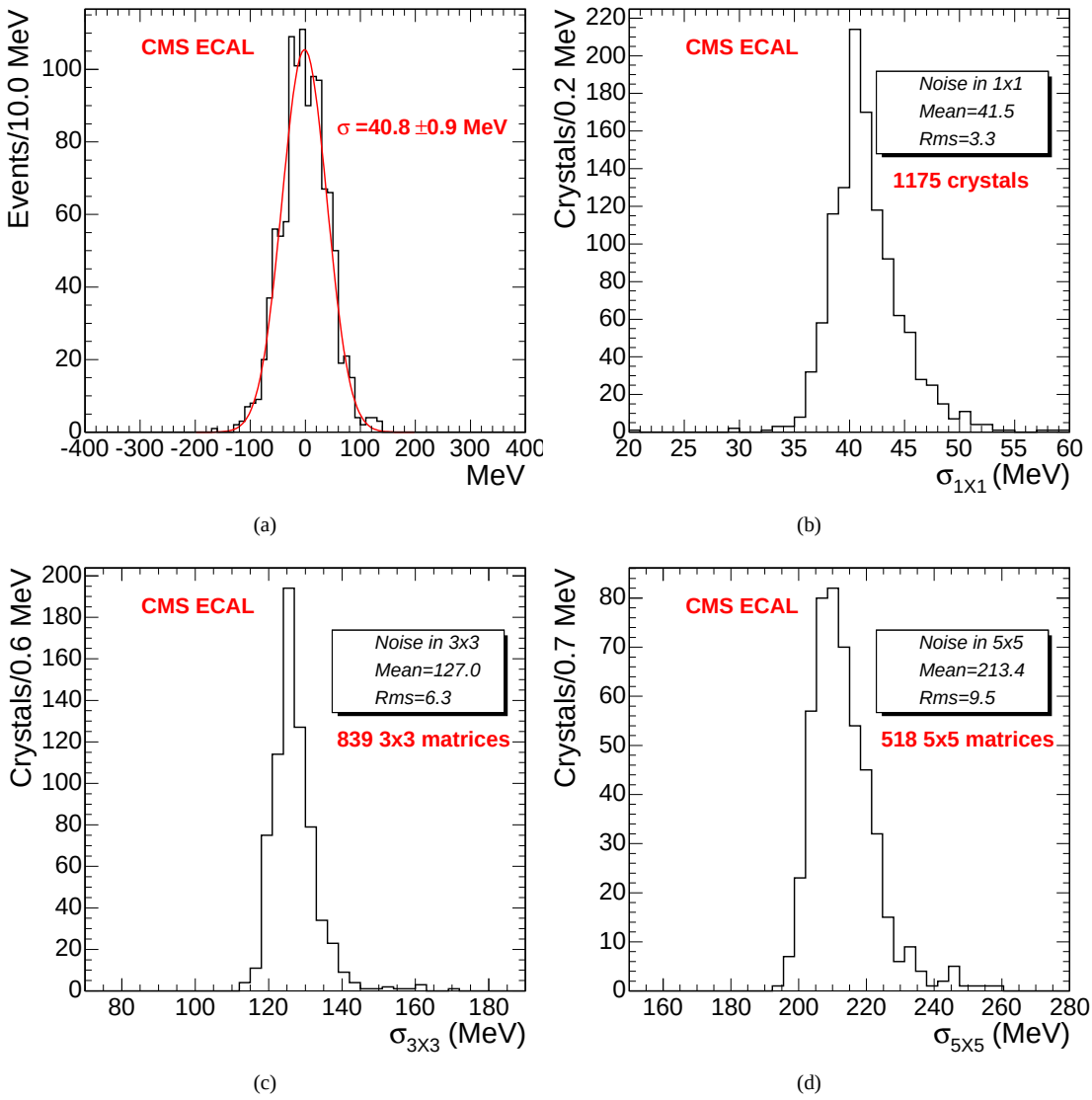

Figure 1: Measurement of the energy-equivalent signal dispersion from electronics noise in individual crystal channels and in matrices of crystals of the ECAL supermodule; a) distribution of the amplitude reconstructed for a single channel; b) distribution of noise measurements in 1175 individual channels; c) distribution of the noise measured in 839 matrices of 3×3 crystals; d) distribution of the noise measured in 518 matrices of 5×5 crystals.

matrices. This corresponds to, respectively, about 3 times and 5 times the single channel noise, as expected in the absence of channel-to-channel correlated noise.

3.2 Determination of gain ratios

All crystal channels are intercalibrated at gain 12 using 120 GeV electrons. A signal amplified by gain 12 saturates the ADC for an energy deposit in an individual crystal of about 140 GeV; this energy deposit in a single crystal can be reached by 160 GeV electrons incident on the centre of the crystal, or by electrons of higher energy for off-centred incidence. In order to reconstruct the energy of electrons with energies above 160 GeV, the ratio of the gains of the MGPA paths with nominal gains 6 and 12 must be determined.

Two different methods were used in dedicated data taking runs to determine the relative gains for each crystal channel, the “Test Pulse” and the “Laser Ramp” methods.

- Test Pulse method: a charge is injected into the MGPA and then sampled by the ADC at a fixed phase, with the gain path forced to a particular choice; the ratio of the reconstructed amplitudes gives the wanted gain ratio.
- Laser Ramp method: a laser ramp is performed by slowly increasing the intensity of laser pulses injected into the crystal by the laser monitoring system [7], with the gain path forced to a particular choice. The ratio of the slopes, measured for different gain paths, corresponds to the wanted gain ratio.

The two methods agree to an accuracy of 0.5 %.

The gain ratio can also be evaluated using electron data. For electrons with energies of e.g. 180 GeV incident on the centre of a crystal, the energy deposited in this crystal fluctuates about the critical value of 140 GeV, depending on the shower development and incident position. As a consequence, the gain path used for this crystal varies from event-to-event, and the energy resolution becomes particularly sensitive to the gain ratio. An example of the variation of the energy resolution for 180 GeV electrons, as a function of the gain ratio, is shown in Fig. 2. The energy measurement uses a 3×3 crystal matrix centred on the incident beam axis, and a shower containment

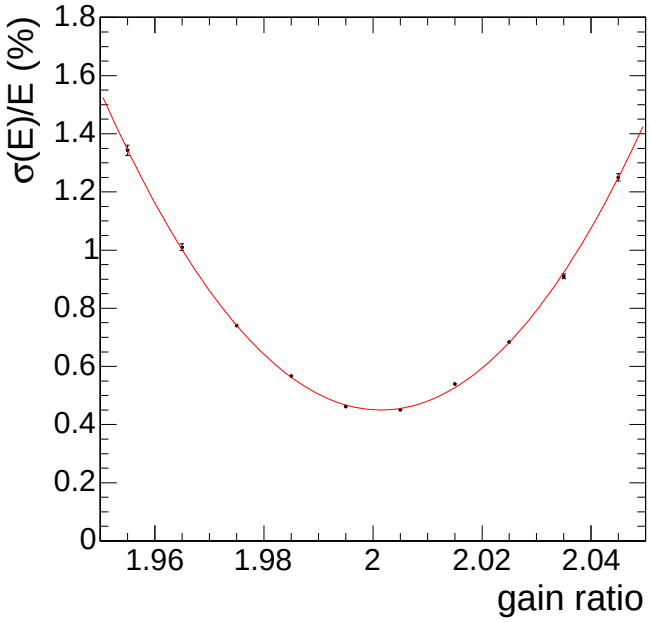

Figure 2: Variation of the energy resolution as a function of the ratio of amplification gains ("gain 12" over "gain 6") for electrons of 180 GeV. The electron beam is incident on crystal 1104 and the measurement is performed in a fixed matrix of 3×3 crystals. Corrections for the position dependence of the shower containment have been applied. A dispersion of 0.14% from beam momentum uncertainty and effects of synchrotron radiation is included.

correction [9] is made as a function of incident position to account for the variation of the amount of energy contained in the matrix. It can be inferred from Fig. 2 that a precision of 0.5 % on the gain ratio, as obtained from the dedicated runs via the Test Pulse and Laser Ramp methods, is insufficient to achieve the best possible energy resolution.

In the following analysis the correct gain ratio for each channel was determined by minimizing the energy resolution for 180 GeV electrons.

4 Energy resolution for central incidence

4.1 Resolution at 120 and 250 GeV

Central incidence is defined as electrons incident within an area of 4×4 mm^2 around the point of maximum shower containment [9]. The energy contained in a finite crystal matrix depends on the electrons' incident position. Investigating the energy resolution with central incidence, with containment losses almost constant, gives a measure of the intrinsic resolution of the calorimeter. However, only 7% of the events taken with the 20×20 mm^2 trigger fall within the central incidence boundaries. In the following, results are given for runs with 30 000 events taken in two crystals located at the same azimuth, but different pseudorapidity, η, in the CMS detector; namely at $\eta = 0.62$ (crystal 704) and $\eta = 0.97$ (crystal 1104).

The energy spectra for 120 and 250 GeV electrons reconstructed in a 3×3 matrix centred on crystals 704 and 1104, are shown in Fig. 3, and for energy reconstructed in a 5×5 matrix in Fig. 4. The energy scale in these plots is obtained by normalizing the mean signal amplitude to the beam momentum. The crystals were intercalibrated

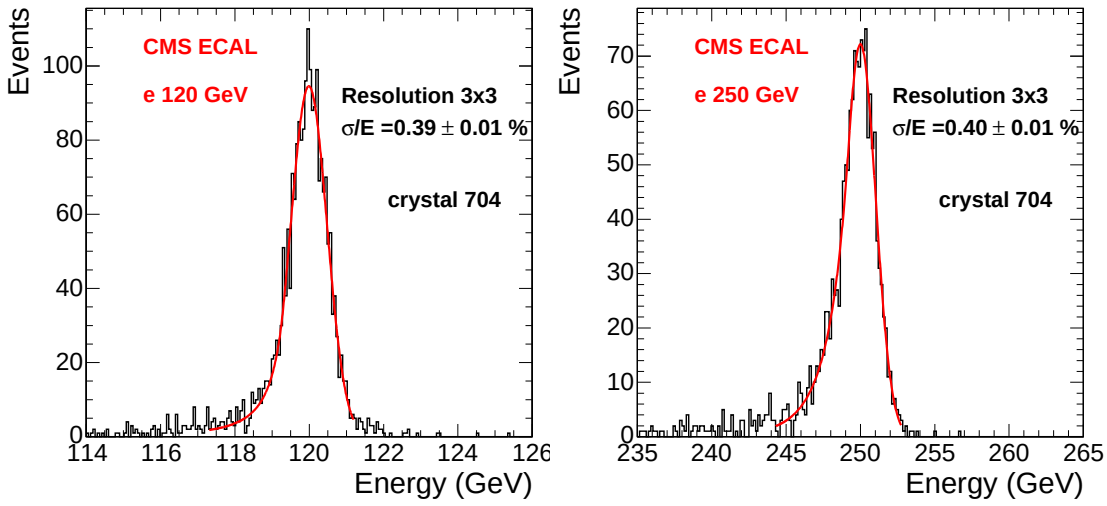

(a)

(b)

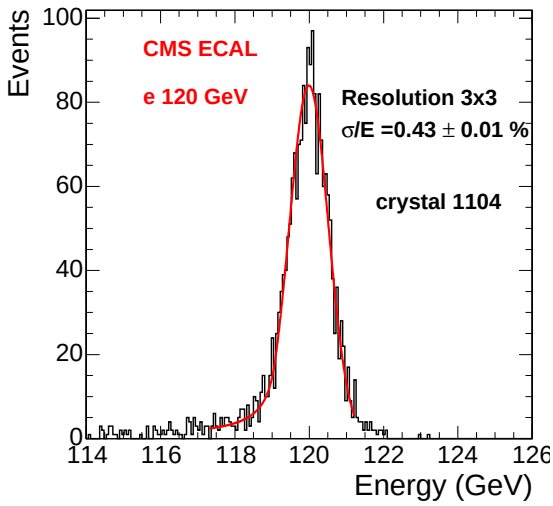

(c)

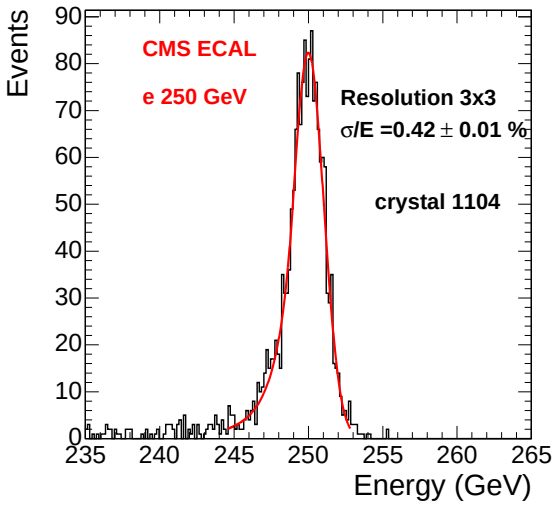

(d)

Figure 3: Distribution of energy reconstructed for central incidence in 3×3 crystal matrices for different central crystals and electron energies; a) 120 GeV electrons on crystal 704; b) 250 GeV electrons on crystal 704; c) 120 GeV electrons on crystal 1104; d) 250 GeV electrons on crystal 1104.

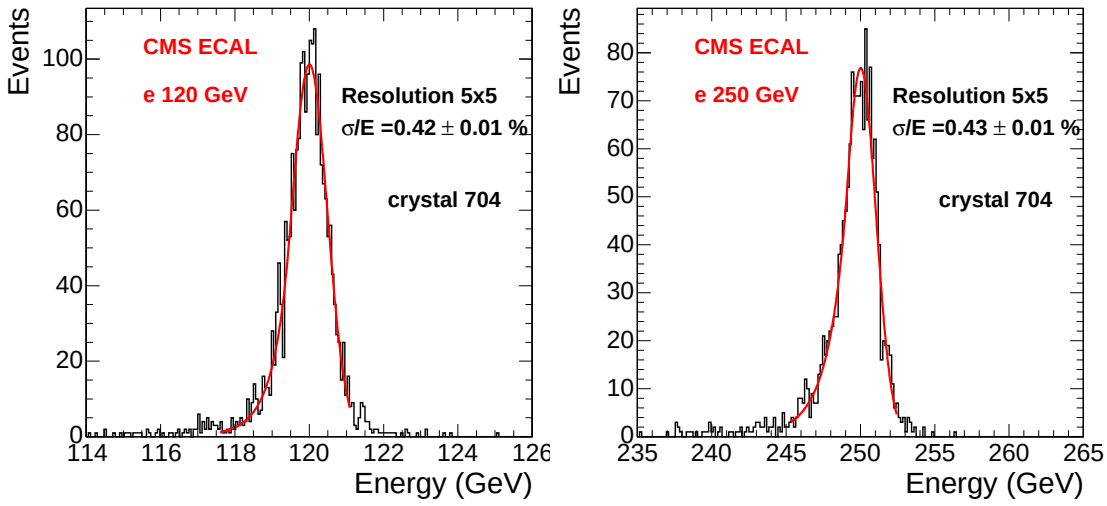

(a)

(b)

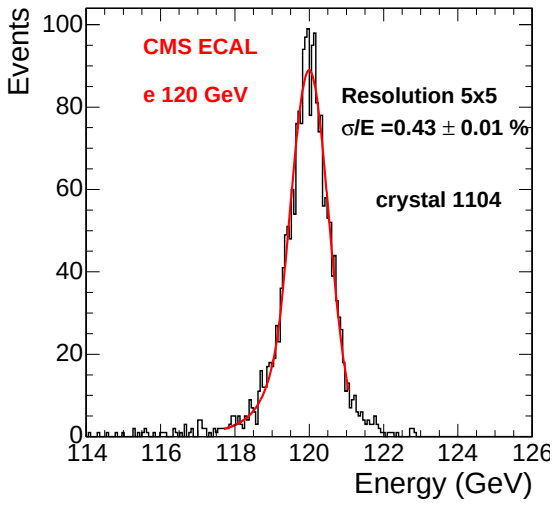

(c)

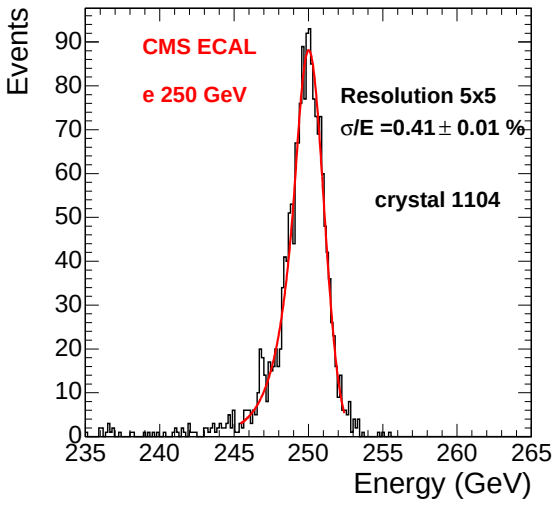

(d)

Figure 4: Distribution of energy reconstructed for central incidence in 5×5 crystal matrices for different central crystals and electron energies; a) 120 GeV electrons on crystal 704; b) 250 GeV electrons on crystal 704; c) 120 GeV electrons on crystal 1104; d) 250 GeV electrons on crystal 1104.

Energy (GeV)	$\sigma_p/p(\%)$
50	~ 0
120	~ 0
150	0.05
180	0.11
250	0.23

Table 1: Root mean square fluctuations in the momentum of electrons in the beam due to synchrotron radiation.

with constants determined directly from the test beam data. The determination of the MGPA gain ratio which is used in the 250 GeV runs, was described in Section 3.2.

A tail towards low energy can be observed in all these distributions. The shape of the signal pulse for the events in the tails is compatible with the expected waveform, which should lead to a correct estimation of the amplitude. However, the number of hodoscope fibres which fired and the corresponding hit patterns suggest that these events might be due to electrons showering upstream in the beam line.

In order to cope with the non-Gaussian distributions, the resolution was determined using a fit with a Gaussian combined with a polynomial tail.

4.2 Beam related effects

The spread of electron momentum in the beam has two main sources. The first is the apertures of the beam collimators placed before and after the momentum defining dipole. The second is synchrotron radiation fluctuations. The percentage spread from the collimator setting is given by the formula

$$\frac{\sigma_p}{p} = \frac{1}{\sqrt{3}} \frac{\sqrt{C_3^2 + C_8^2}}{27} \; ; \tag{1}$$

where C_3 and C_8 are the half-widths (in mm) of the two collimators. Both half-widths are about 3 mm giving a spread in the beam momentum of roughly 0.09% at all energies.

The Table 1 shows the values of the synchrotron radiation fluctuations for increasing values of the beam energy. These numbers have been calculated using a Monte Carlo simulation of the beam [10]. The overall uncertainty on the electron energy due to synchrotron radiation is non-negligible only towards high energies. The energy resolution obtained for central incidence after quadratic subtraction of the beam momentum spread is summarized in Table 2.

	$\sigma_E/E(\%)$ for Crystal 704			$\sigma_E/E(\%)$ for Crystal 1104		
Crystal Matrix	Fit of Raw Results	p spread subtracted	p spread & radiation subtracted	Fit of Raw Results	p spread subtracted	p spread & radiation subtracted
	E = 120 GeV					
3×3	0.39	0.38	0.38	0.43	0.42	0.42
5×5	0.42	0.41	0.41	0.43	0.42	0.42
	E = 250 GeV					
3×3	0.40	0.39	0.33	0.42	0.41	0.34
5×5	0.43	0.42	0.35	0.41	0.40	0.33

Table 2: Energy resolutions in 3×3 and 5×5 crystal matrices. The results obtained from the fits shown in Figs. 3 and 4 are summarized in the first column. The results obtained after subtracting the beam momentum spread are shown in the second column. The final results after subtracting both the beam momentum spread and the synchrotron radiation fluctuations are shown in the last column. The errors on these numbers are roughly ± 0.01.

The systematic error on the beam momentum spread is quite large. Relative errors of 10% on the spread coming from the collimator settings and of 50% on the spread coming from the synchrotron radiation fluctuations are used in the following for functional fits to the resolution as a function of beam energy. Both types of systematic errors are assumed to be fully correlated between energy points.

4.3 Resolution as a function of energy

The energy dependence of the energy resolution is studied for data taken at 20, 30, 50, 80, 120, 180 and 250 GeV. The energy dependence is fitted by the following functional form:

$$\left(\frac{\sigma}{E}\right)^2 = \left(\frac{S}{\sqrt{E}}\right)^2 + \left(\frac{N}{E}\right)^2 + C^2 \qquad (E \text{ in GeV}) \tag{2}$$

where S is the stochastic term, N the noise and C the constant term. The fit is performed with the noise term fixed for each crystal at the value measured in the pedestal runs.

The energy resolution for 3×3 matrices centred on crystal 704 and on 1104 are shown in Fig. 5, together with the fitted resolution function curves. The error bars include both statistical and systematic errors, with the

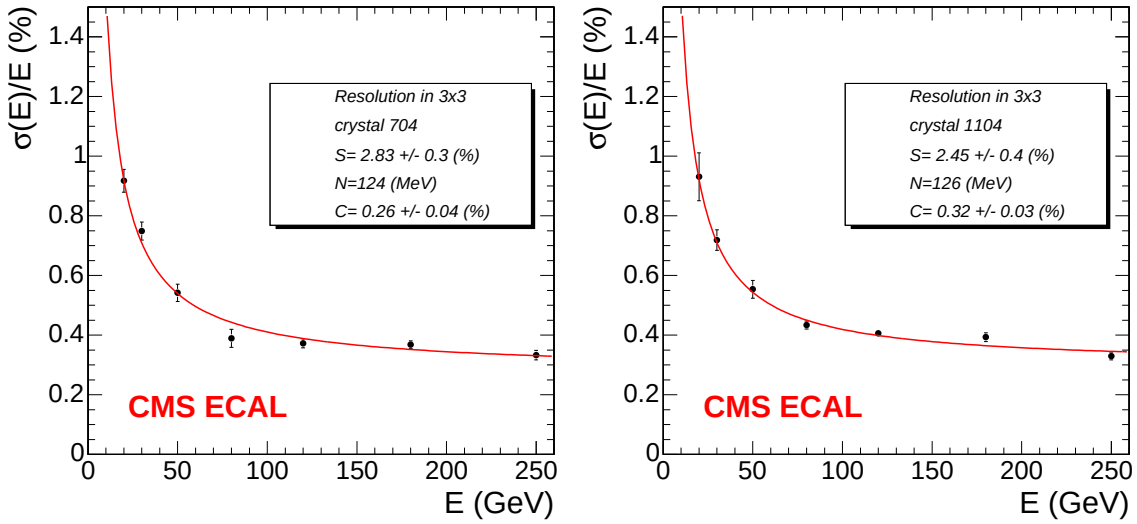

(a) (b)

Figure 5: Resolution as a function of the energy reconstructed by summing in 3×3 crystals centred on a) crystal 704 and b) on crystal 1104, with beam hodoscope cuts of $4 \times 4\text{mm}^2$.

statistical uncertainties becoming large at the lower energies. The constant terms are around 0.3%.

The resolution as a function of energy for 18 different positions of the 3×3 matrices is shown in Fig. 6. The results are obtained for data taken when the beam is centred on each crystal of two sets of nine crystals, including the reference crystals (704 and 1104) and their eight neighbours. The mean of the 18 values of energy resolution at each energy are listed in Table 3.

Energy (GeV)	Resolution (%)
20	0.94 ± 0.05
30	0.74 ± 0.04
50	0.56 ± 0.03
80	0.45 ± 0.02
120	0.40 ± 0.01
180	0.38 ± 0.01
250	0.34 ± 0.01

Table 3: Mean values of the energy resolution obtained in matrices of 3×3 crystals centred on 18 different crystals. The results are presented for various incident beam energies. The beam spread contributions have been subtracted.

Figures 7a and 7b show the 18 values of stochastic and constant terms obtained from the 18 fits performed on the data shown in Fig. 6. The error bars represent the total error on these parameters, the dominant one being the statistical error. The mean value of the stochastic term is around 2.8% and the mean value of the constant term is around 0.30%. The global dispersion of both parameters is dominated by the uncertainties. Thus, each crystal's term is compatible with average value.

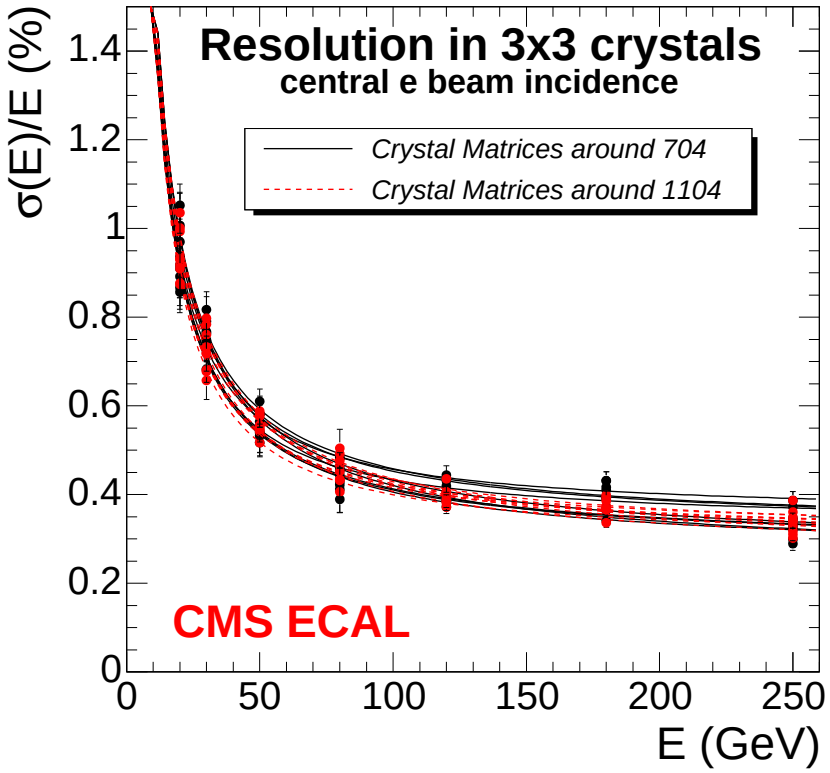

Figure 6: Resolution as a function of the energy reconstructed by summing matrices of 3×3 crystals. The plot shows the resolution obtained for 18 different central crystals after applying the beam hodoscope cuts of $4 \times 4\,\mathrm{mm}^2$.

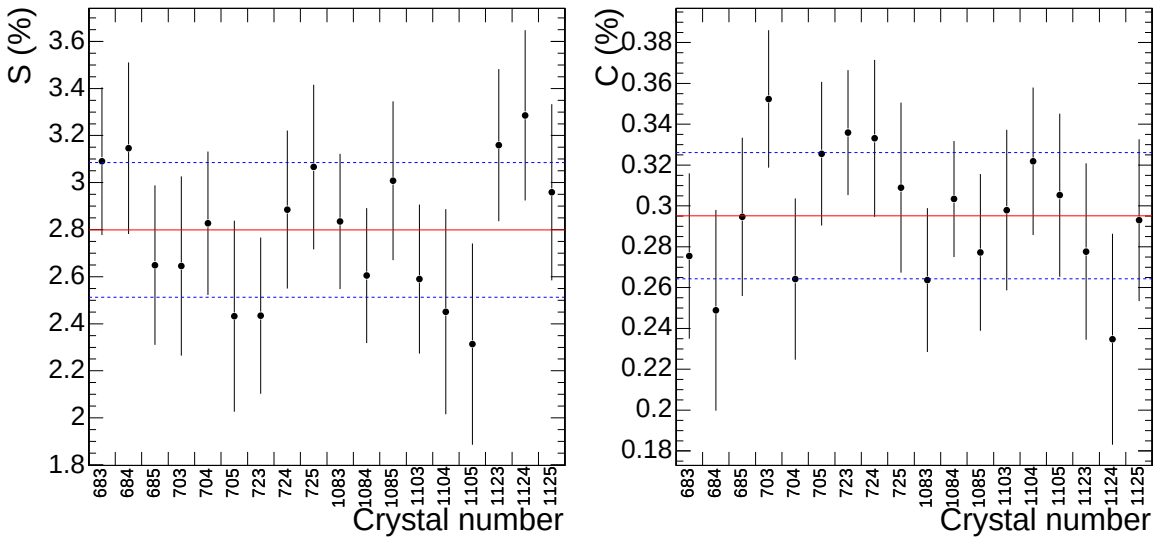

(a) (b)

Figure 7: a) Stochastic term obtained for 18 crystals. b) Constant term obtained for 18 crystals. The average values are represented by the lines and the dashed lines correspond to $\pm 1\sigma$.

5 Energy resolution for uniform incidence

5.1 Resolution at 120 GeV

In this section the data from all electrons in the 20×20 mm^2 trigger are used. The trigger is roughly centred (± 3 mm) on the point of maximum response of a crystal. Figure 8 shows the beam profile for a typical run. These profiles give a rather uniform distribution of the beam over the front faces of the crystals. The reconstructed energy

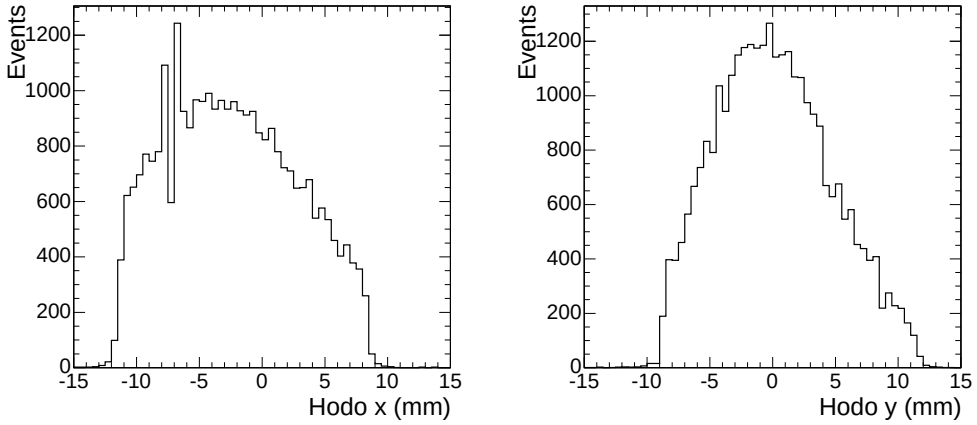

(a) (b)

Figure 8: Beam profile at 120 GeV measured by the hodoscope in: a) the horizontal (x) direction; and b) the vertical (y) direction.

varies with the position of the incident electron. A method using only the distribution over the crystal matrix of the energy deposited in the crystals has been developed to correct for the dependence on incident position. A single parametrized function of each transverse coordinate is used for correction in all parts of the supermodule [9].

Figure 9 shows the distribution of energy reconstructed at 120 GeV in 3×3 and 5×5 matrices of crystals centred on crystal 704 and 1104 for all triggered electrons when the method described above is used to correct for the energy containment variation.

5.2 Resolution as a function of energy

The resolution as a function of energy is extracted for the case of uniform incidence with the shower containment corrections described in a previous section applied. The functional form of Eq. 2 is used.

Figure 10 shows, for the 3×3 matrix centred on crystal 1104, the squared fractional energy resolution after subtraction of the squared fractional measured noise plotted against the reciprocal of the beam energy. A straight line is fitted to extract the values of the stochastic and constant terms.

Figure 11 shows the energy resolution as a function of energy when summing either 3×3 or 5×5 matrices, with the beam directed either on crystal 704 (Fig. 11a) or on crystal 1104 (Fig. 11b). The errors quoted on the fitted parameters include both the statistical and the estimated systematic uncertainties discussed in Section 4.2. The resolution is better than 0.5% for electrons of energy greater than 100 GeV. Compared to the results obtained for central incidence (Fig. 5) a slight increase of the stochastic term is observed.

The fitted resolution as a function of energy is shown in Fig. 12 for 18 different positions of the 3×3 matrices. The results are obtained for data taken when the beam is directed on each crystal of two sets of nine crystals, including the reference crystals (704 and 1104) and their eight neighbours. Compared to the results obtained for central incidence (Fig. 6) a slightly larger dispersion of the stochastic and constant terms is observed.

6 Conclusion

Test beam data taken in 2004 allowed exhaustive performance studies to be made on one CMS ECAL supermodule.

A noise level of 41 MeV per channel is observed. The average value of the total noise summed in matrices of 3×3 and 5×5 crystals is found to be respectively 127 MeV and 213 MeV. These averages are obtained from roughly 900 different summed matrices.

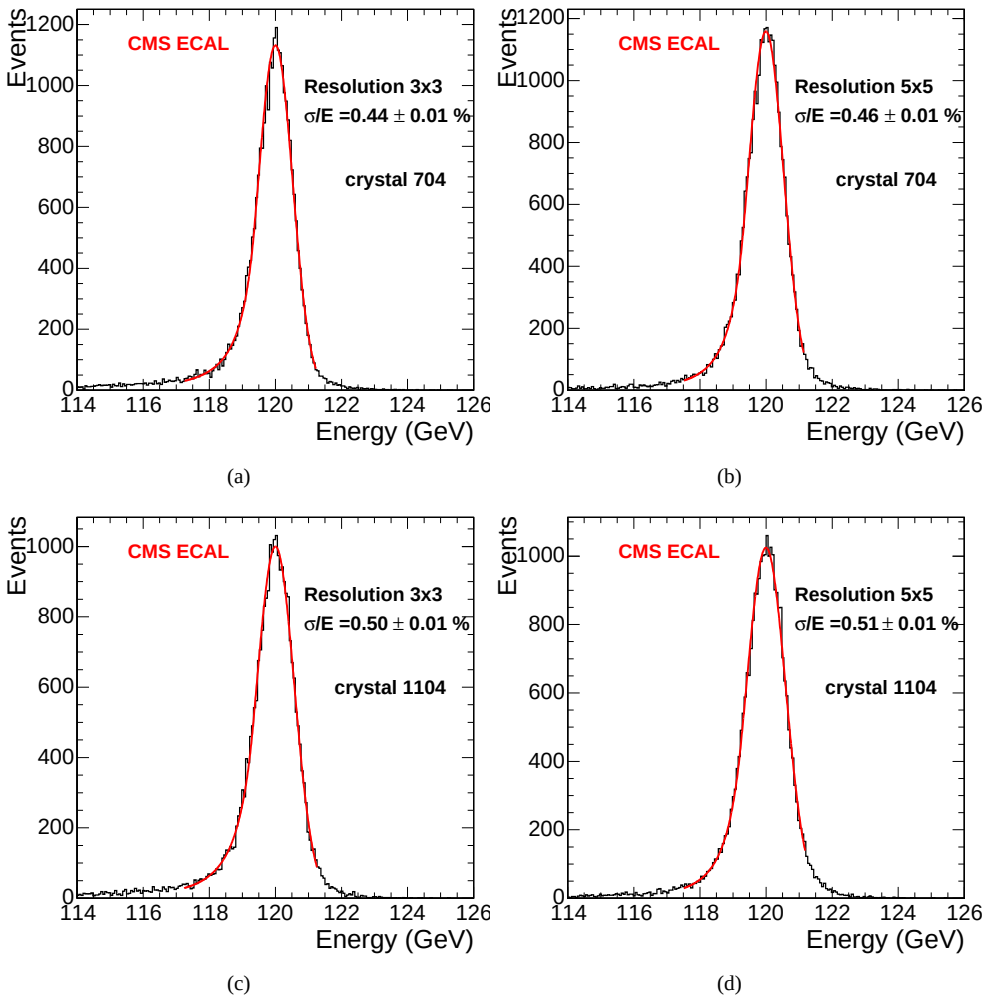

Figure 9: Distribution of energy reconstructed for electrons at 120 GeV with uniform incidence on the central crystal and measured in a) 3×3 crystals centred on crystal 704; b) 5×5 crystals centred on crystal 704; c) 3×3 crystals centred on crystal 1104; d) 5×5 crystals centred on crystal 1104.

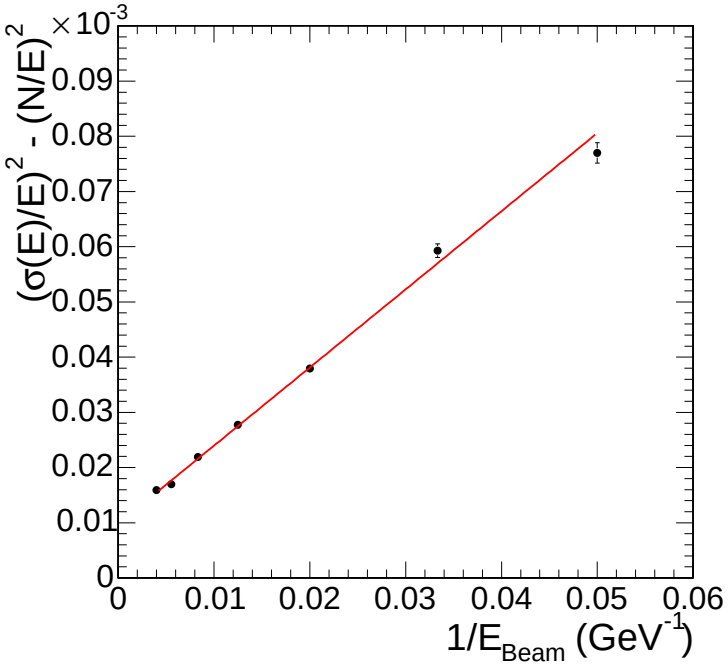

Figure 10: $\left(\frac{\sigma}{E}\right)^2 - \left(\frac{N}{E}\right)^2$ as a function of the reciprocal of the beam energy. The resolution is for a sum of 3×3 crystals centred on crystal 1104.

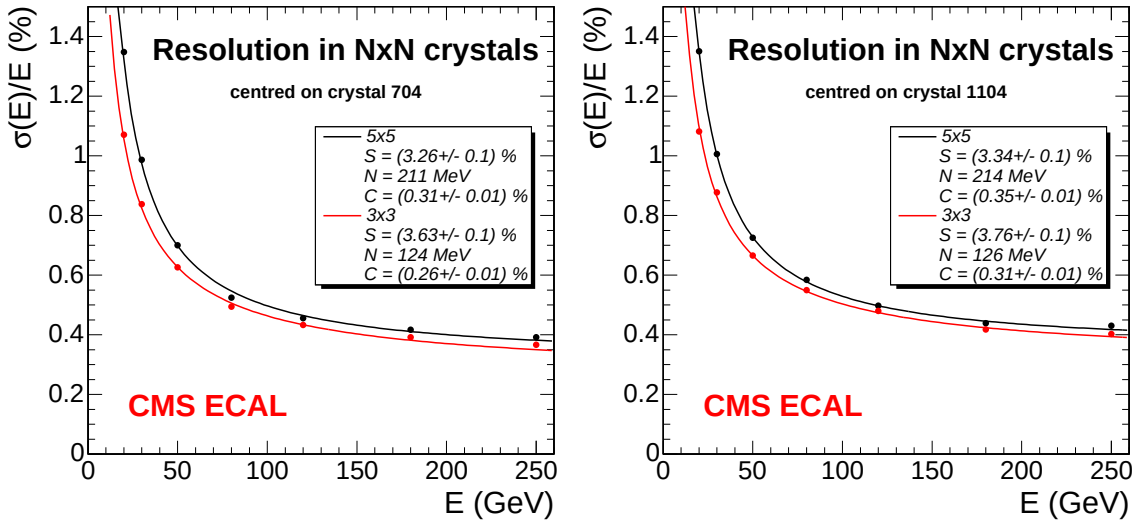

(a) (b)

Figure 11: Resolution as a function of the energy reconstructed by summing 5×5 crystals compared to the sum of 3×3 crystals centred on the a) crystal 704 and b) crystal 1104.

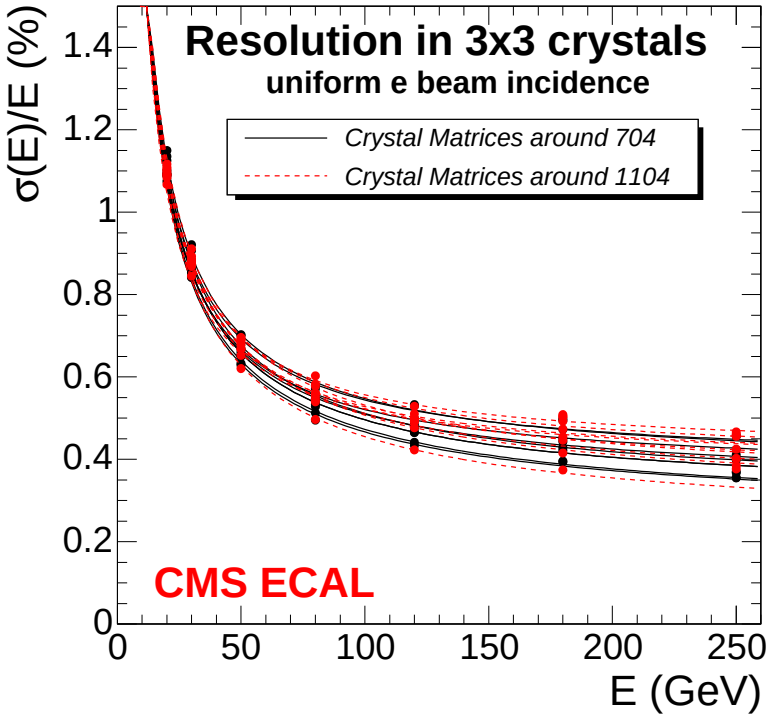

Figure 12: Resolution as a function of the energy reconstructed by summing in 3×3 crystals. The plot shows the resolution obtained for 18 different central crystals.

Consistent energy resolution is obtained for electrons with incidence in different areas of the supermodule. For a beam with central incidence on 18 different crystals and after subtraction of the beam spread, the average resolution obtained for electrons of 120 GeV is 0.40±0.01% when using energy reconstructed by summing 3×3 crystals. A typical energy dependent resolution function obtained for such central incidence is:

$$\left(\frac{\sigma}{E}\right)^2 = \left(\frac{2.8\%}{\sqrt{E}}\right)^2 + \left(\frac{.125}{E}\right)^2 + (0.30\%)^2 \qquad (E \text{ in GeV}) \tag{3}$$

A coherent set of resolution functions are obtained for the 18 cases with stochastic and constant terms having a relative dispersion of 10% around their central values.

For a uniform beam incidence, after correcting for the dependence of the reconstructed energy on incident position, only a slight increase of the stochastic term has been observed. The average energy resolution in the 18 crystal matrices is found to be better than 0.5% for electrons above 100 GeV, both for energies reconstructed in 3×3 and in 5×5 crystal matrices.

The performance of a fully equipped CMS ECAL supermodule meets the design target for energy resolution and noise level.

7 Acknowledgments

We would like to thank the technical staff from the collaborating laboratories and institutions who have helped in the preparation of the test beam campaign. Our thanks go also to the CERN staff for their support and operation of the accelerator delivering the beam at the H4 testing Hall.

References

[1] CMS Collaboration, “The Compact Muon Solenoid - Technical Proposal”, CERN/LHCC 94-38 (December 1994) 290pp.

[2] CMS Collaboration, “The Electromagnetic Calorimeter Project”, Technical Design Report, CERN/LHCC 97-23 (15 December 1997) 364pp.

[3] CMS Collaboration, “CMS Physics Technical Design Report Vol. 1”, CERN/LHCC 2006-001 (February 2006) 547pp.

[4] CMS Ecal Electromagnetic Calorimeter Group, P. Adzic et al., “Results of the first performance tests of the CMS electromagnetic calorimeter”, Eur. Phys. J. C44 S2 (2006) 1-10.

[5] P. Milenovic et al., “Performance of the CMS ECAL safety system for Super Modules SM0 and SM1”, Nucl. Instrum. Meth.A554 (2005) 427-436.

[6] P. Adzic et al., “The detector control system for the electromagnetic calorimeter of the CMS experiment at the LHC”, CERN-CMS-CR-2005-028
Prepared for 10th International Conference on Accelerator and Large Experimental Physics Control Systems (ICALEPCS 2005), Geneva, Switzerland, 10-15 Oct 2005.

[7] L. Zhang et al., “Performance of the Monitoring Light Source for the CMS Lead Tungstate Crystal Calorimeter”, IEEE Trans. Nucl.Sci. 52 (2005) 1123-1130.

[8] CMS Ecal Electromagnetic Calorimeter Group, P. Adzic et al., “Reconstruction of the signal amplitude of the CMS electromagnetic calorimeter”, Eur. Phys. J. C46 S1 (2006) 23-35.

[9] J. Descamps and P. Jarry, “Correction for the periodic position dependence of the energy deposited in fixed size matrices of crystals in the CMS Barrel electromagnetic calorimeter”, CMS Note 2006/045.

[10] P. Grafström, “The momentum resolution of the H4 beam for secondary beams in Filter Mode optics”, CERN Accelerator and Beams SL-Note-97-81/EA (December 1997) 7 pp.